

Optical modulation and fabrication of two-dimensional VO_2(M)-$AgSiO_2$ shell/core composite photonic crystal structures

Jiong Wu(吴炯), Zhangyang Zhou(周章洋), Li Zhu(朱黎), Liushun Wang(王六顺), Ming Du(杜明), Hongjun Wu(吴红君), Qingwei Wang(王情伟), Dahua Ren(任达华), Teng Zhang(张腾), Yongdan Zhu(朱永丹), and Jinqiao Yi(易金桥)

Citation: Chin. Phys. B, 2026, 35 (**4**): 046802. DOI: 10.1088/1674-1056/ae1569
http://cpb.iphy.ac.cn; http://iopscience.iop.org/cpb

What follows is a list of articles you may be interested in

High-energy x-ray diffraction study on phase transition asymmetry of plastic crystal neopentylglycol

Zhe Zhang(张哲), Yan-Na Chen(陈艳娜), Ji Qi(齐迹), Zhao Zhang(张召), Koji Ohara, Osami Sakata, Zhi-Dong Zhang(张志东), and Bing Li(李昺)
Chin. Phys. B, 2022, 31 (**3**): 036802. DOI: 10.1088/1674-1056/ac140c

Manipulating metal-insulator transitions of VO_2 films via embedding Ag nanonet arrays

Zhangyang Zhou(周章洋), Jia Yang(杨佳), Yi Liu(刘艺), Zhipeng Gao(高志鹏), Linhong Cao(曹林洪), Leiming Fang(房雷鸣), Hongliang He(贺红亮), and Zhengwei Xiong(熊政伟)
Chin. Phys. B, 2021, 30 (**12**): 126803. DOI: 10.1088/1674-1056/ac003a

Phase transition-induced superstructures of *β*-Sn films with atomic-scale thickness

Le Lei(雷乐), Feiyue Cao(曹飞跃), Shuya Xing(邢淑雅), Haoyu Dong(董皓宇), Jianfeng Guo(郭剑锋), Shangzhi Gu(顾尚志), Yanyan Geng(耿燕燕), Shuo Mi(米烁), Hanxiang Wu(吴翰翔), Fei Pang(庞斐), Rui Xu(许瑞), Wei Ji(季威), and Zhihai Cheng(程志海)
Chin. Phys. B, 2021, 30 (**9**): 096804. DOI: 10.1088/1674-1056/ac11e8

Probing thermal properties of vanadium dioxide thin films by time-domain thermoreflectance without metal film

Qing-Jian Lu(陆青鑑), Min Gao(高敏), Chang Lu(路畅), Fei Long(龙飞), Tai-Song Pan(潘泰松), and Yuan Lin(林媛)
Chin. Phys. B, 2021, 30 (**9**): 096801. DOI: 10.1088/1674-1056/abea94

Fabrication of VO_2 thin film by rapid thermal annealing in oxygen atmosphere and its metal-insulator phase transition properties

Liang Ji-Ran (梁继然), Wu Mai-Jun (吴励君), Hu Ming (胡明), Liu Jian (刘剑), Zhu Nai-Wei (朱乃伟), Xia Xiao-Xu (夏晓旭), Chen Hong-Da (陈弘达)
Chin. Phys. B, 2014, 23 (**7**): 076801. DOI: 10.1088/1674-1056/23/7/076801

Optical modulation and fabrication of two-dimensional VO_2(M)-$AgSiO_2$ shell/core composite photonic crystal structures

Jiong Wu(吴炯)[1], Zhangyang Zhou(周章洋)[1,†], Li Zhu(朱黎)[1], Liushun Wang(王六顺)[1], Ming Du(杜明)[1], Hongjun Wu(吴红君)[2], Qingwei Wang(王情伟)[1], Dahua Ren(任达华)[1], Teng Zhang(张腾)[1], Yongdan Zhu(朱永丹)[1], and Jinqiao Yi(易金桥)[1,‡]

[1] *College of Intelligent Systems Science and Engineering, Hubei Minzu University, Enshi* 445000, *China*
[2] *School of Chemistry and Environmental Engineering, Hubei Minzu University, Enshi* 445000, *China*

(Received 13 August 2025; revised manuscript received 15 October 2025; accepted manuscript online 21 October 2025)

The high phase transition temperature, low solar modulation efficiency, and unfavorable brown-yellow color have limited the practical application of VO_2-based smart windows. By embedding a hexagonal close-packed monolayer array of SiO_2 into the monoclinic VO_2(M)–Ag composite film using an electron-beam evaporation system, a two-dimensional VO_2(M)–$AgSiO_2$ shell/core photonic crystal composite material was formed. Due to the increased contact area between Ag and VO_2(M) within the composite material, the concentration of free electrons in VO_2(M) increases, causing the phase transition to occur at a lower temperature of 52.2 °C. With the embedded SiO_2 array, the solar modulation efficiency is enhanced to 25.4%, and the visible light modulation efficiency increases by nearly 7 times. Additionally, the grating effect of the photonic crystal significantly diffracts light around the 600 nm wavelength, reducing the strong absorption of VO_2(M) in the shortwave range and diluting its inherent brown-yellow color. By embedding the SiO_2 array into the VO_2(M)–Ag composite film, this approach simultaneously achieves a reduction in phase transition temperature, enhancement of solar modulation efficiency, and color adjustment of the film, providing a reference for the practical application of VO_2 in smart windows.

Keywords: vanadium dioxide, photonic crystal, phase transition, solar modulation efficiency

PACS: 68.03.–g, 68.35.–p

DOI: 10.1088/1674-1056/ae1569 **CSTR:** 32038.14.CPB.ae1569

1. Introduction

Smart windows play an essential role in building energy efficiency. In hot weather, they effectively block substantial sunlight; while in colder seasons, they allow solar energy to pass through, helping to regulate indoor temperatures.[1,2] Thermochromic smart windows, which adjust solar transmission based on temperature, have been extensively researched in recent years and have become an important component of green buildings. Vanadium dioxide (VO_2) is a typical thermochromic material that undergoes an insulator-to-metal phase transition at approximately 341 K.[3–6] The transition is accompanied by a sharp decrease in infrared transmittance while maintaining high transmittance in the visible range.[6] Consequently, VO_2-based thermochromic windows could significantly reduce solar heat gain at high temperatures without affecting indoor brightness.[3–5] However, the high transition temperature (T_c), low solar modulation efficiency (ΔT_{sol}), and unfavorable brown-yellow color have limited the practical application of VO_2-based smart windows.[3–8]

Researchers have proposed various methods to address these challenges, including element doping,[9–11] composite structures,[12–16] porous structures,[17,18] multilayer structures,[19,20] and core-shell structures.[21–23] Elemental doping or compositing can effectively reduce the T_c, but this often comes at the expense of ΔT_{sol}.[9–11] Fabricating VO_2 in porous structures or adding anti-reflective layers can increase optical transmittance and enhance the ΔT_{sol}, yet these approaches do not lower T_c and are further limited by complex fabrication processes.[12–20] Recently, Ke *et al.* embedded VO_2 within a monolayer hexagonal array of SiO_2 spheres to form a SiO_2/VO_2 core-shell structure. By adjusting the size of the SiO_2 spheres, control over the film color and ΔT_{sol} was achieved, but the T_c was not effectively reduced.[21] To date, low T_c, high ΔT_{sol} and desirable color have yet to be simultaneously achieved, indicating a continued need for further research.

A monolayer-based, two-dimensional periodic nanostructure of colloidal spheres can be viewed as a two-dimensional photonic crystal.[20–23] By adjusting the structural parameters of the photonic crystal, specific wavelengths of visible light can be inhibited, thereby altering the color of the material.[24–27] Furthermore, extensive research has demonstrated that incorporating noble metals (e.g., Pt, Ag) into VO_2 films can lower T_c by increasing free electron density.[12,28–31]

[†]Corresponding author. E-mail: zhangyangzhou0000@163.com
[‡]Corresponding author. E-mail: 2006009@hbmzu.edu.cn

© 2026 Chinese Physical Society and IOP Publishing Ltd. All rights, including for text and data mining, AI training, and similar technologies, are reserved.

Consequently, combining a VO_2–Ag composite film with a monolayer SiO_2 colloidal sphere array might enable T_c reduction, improved ΔT_{sol}, and better control over the film color.

In this study, SiO_2 nanoarrays were embedded into the monoclinic VO_2(M)–Ag composite film using an SiO_2 template and electron-beam evaporation system to study the optical properties of the composite film.

2. Experimental details

2.1. Preparation of all samples

A monolayer, dense SiO_2 nanoarray was prepared using an improved interfacial self-assembly method (Figs. 1(a)–1(d)).[32,33] Briefly, the 0.3 wt% SiO_2 colloidal spheres (500 nm) were dispersed in a 1:1 volume ratio mixture of deionized water and absolute ethanol, and then slowly dripped onto a water/air interface via drainage glass to form a single layer of dispersed SiO_2 nanospheres (Fig. 1(a)). Then, several drops of 2 wt% sodium dodecyl benzene sulfonate solution were added to drive the floating SiO_2 spheres to form a rainbow film (Fig. 1(b)). Next, the monolayer of SiO_2 colloidal spheres was transferred onto a clean quartz substrate using a PTL-MMB01 dip-coating machine (Shenyang Kejing) at a lifting speed of 120 μm/min (Fig. 1(c)), and then we obtained the regulated SiO_2 photonic crystal (Fig. 1(d)).

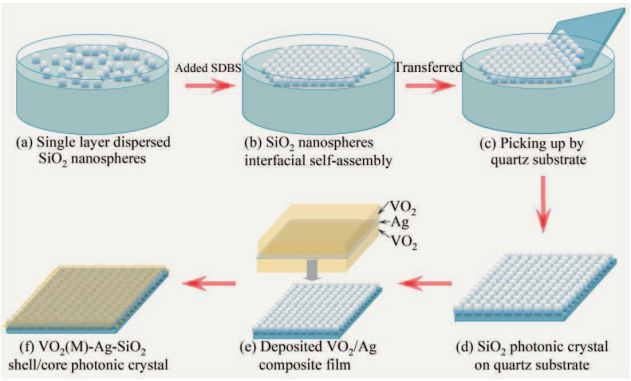


Fig. 1. Schematic diagram of the procedure to fabricate VO_2(M)–Ag–SiO_2 shell/core photonic crystal composite films. (a)–(d) Fabrication of SiO_2 photonic crystal, and (e) and (f) preparation of VO_2(M)–Ag–SiO_2 shell/core composite films.

The preparation methods of VO_2 films have been previously reported.[12,34,35] The VO_2 films were prepared using the electron-beam evaporation system at a base pressure 5.0×10^{-5} Pa. Under high vacuum conditions (working pressure 5×10^{-3} Pa), the VO_2 target was placed in a crucible located ~ 300 mm below the substrate holder and evaporated by an incident electron beam with an accelerating voltage of 10 kV. On a quartz substrate heated to 300 °C, a VO_2 film with a thickness of 200 nm was grown at a deposition rate not exceeding 0.5 nm/s. For the preparation of composite films, a clean quartz substrate and a quartz substrate with an SiO_2 array were simultaneously placed on the substrate holder. A 90 nm thick VO_2 film was first deposited on both substrates using the same growth process. Then, an Ag layer with a thickness of 20 nm was deposited on both samples at a rate not exceeding 0.5 nm/s, followed by another 90 nm thick VO_2 layer (Figs. 1(e) and 1(f)). Research shows that monoclinic VO_2 (VO_2(M)) films with a high (011) orientation in their insulating state exhibit excellent phase transition properties, making them highly suitable for smart coating applications.[36] To achieve optimal film quality, the growth process requires samples to undergo *in-situ* annealing at 500 °C and 10 Pa for 30 minutes. The final products, pure VO_2(M), VO_2(M)–Ag, and VO_2(M)–$AgSiO_2$ composites, are designated as samples S_1, S_2, and S_3, respectively.

2.2. Characterization

The surface morphology of the samples was characterized using a field-emission scanning electron microscope (FESEM, Carl Zeiss Supra VP55, Germany) at an accelerating voltage of 10 kV. The crystal structure of the samples was identified by grazing incidence x-ray diffraction (GIXRD, X'Pert Pro MPD, Netherlands) with Cu $K\alpha_1$ radiation ($\lambda = 0.15406$ nm) at an incidence angle of 1°. Optical transmittance at a fixed wavelength of 2000 nm was measured during heating and cooling in the temperature range of 30 °C to 85 °C using a Shimadzu UV-3700 double-beam UV-Vis-NIR spectrophotometer (Japan) equipped with a temperature control device. Transmittance spectra at 25 °C and 90 °C and absorbance spectra at 25 °C were measured over the wavelength range of 350–2500 nm. The carrier concentration was determined at room temperature using single-magnetic-field (0.58 T) Hall measurements (Nanometrics HL5500PC, USA) based on the van der Pauw method.

2.3. Calculation of optical properties

The solar transmittance (T_{sol}, wavelength range 350–2500 nm) and visible light transmittance (T_{lum}, wavelength range 380–780 nm) of the samples were calculated using the following formulas:[13,17]

$$T_{sol} = \frac{\int \varphi_{sol}(\lambda) T(\lambda) \, d\lambda}{\int \varphi_{sol}(\lambda) \, d\lambda}, \tag{1}$$

$$T_{lum} = \frac{\int \varphi_{lum}(\lambda) T(\lambda) \, d\lambda}{\int \varphi_{lum}(\lambda) \, d\lambda}, \tag{2}$$

while $T(\lambda)$ represents the transmittance spectrum percentage at wavelength λ. $\varphi_{lum}(\lambda)$ is the luminous efficiency function of the human eye under standard photopic vision, and $\varphi_{sol}(\lambda)$ is the solar irradiance spectrum function at an air mass of 1.5 (equivalent to solar irradiance at a 37° angle above the horizon). The ΔT_{sol} and visible light modulation efficiency (ΔT_{lum})

can be calculated using[13]

$$\Delta T_{\mathrm{sol/lum}} = T_{\mathrm{sol/lum}}(90^\circ) - T_{\mathrm{sol/lum}}(25^\circ). \quad (3)$$

3. Results and discussion

Figure 2 shows the GIXRD diffraction patterns of the samples at room temperature. Sample S_1 exhibits a VO_2 film with a pure monoclinic phase and (011) crystal orientation, with diffraction peaks observed at $2\theta \approx 27.9^\circ$, 37.1°, 55.6°, and 57.5°, corresponding to the (011), ($\bar{2}11$), (220), and (022) planes of VO_2(M) ($P2_1/c$, JCPDS#65-2358), respectively.[35] No diffraction peaks from other vanadium oxides were detected, indicating that the film is single-phase within the sensitivity limits of the technique. After the addition of Ag (S_2), new diffraction peaks appear at $2\theta \approx 38.2^\circ$, 44.4°, and 64.6°, corresponding to the (111), (200) and (220) planes of Ag ($Fm\bar{3}m$, JCPDS#87-0720).[12] Following the incorporation of a monolayer hexagonal close-packed SiO_2 nanosphere array (S_3), a new broad peak emerges around $2\theta \approx 23^\circ$, corresponding to amorphous SiO_2. The indicates that VO_2(M)–Ag composite film was successfully deposited onto the SiO_2 nanosphere array.

Figures 3(a) and 3(b) present the microscopic nanostructures of samples S_1 and S_2, respectively, showing a uniform coating of VO_2 nanoparticles on the quartz substrate. The S_1 exhibits well-defined grains with fine cracks and an average grain size of approximately 35 nm. The distinctive structure enhances light transmission, thereby improving the optical properties of the VO_2 film.[13] With the addition of Ag, the fine cracks are eliminated, resulting in a smooth and dense film surface, while the average grain size remains nearly unchanged. Analysis of the EDS spectra from the selected regions of the samples (Figs. 3(c) and 3(d)) reveals an additional resonance peak near 3 keV in Fig. 3(d), which is absent in Fig. 3(c). This new peak corresponds to Ag, confirming the successful incorporation of Ag into the VO_2 thin film. Figure 3(e) shows the prepared SiO_2 nanosphere array, with the nanospheres arranged in a densely packed hexagonal pattern, forming a monolayer structure on the quartz substrate. Each SiO_2 sphere has a uniform diameter of 500 nm. The VO_2(M)–Ag composite film was then deposited onto the SiO_2 template, resulting in the VO_2(M)–Ag–SiO_2 composite film, as shown in Fig. 3(f). The VO_2(M)–Ag composite film uniformly covers the upper portion of the SiO_2 template. The inset in Fig. 3(f) further reveals that the composite material successfully penetrates into the lower spaces between the SiO_2 spheres and the quartz substrate. Building on this, we successfully embedded a monolayer hexagonally close-packed SiO_2 nanosphere array with a particle diameter of 500 nm into the VO_2(M)–Ag composite, forming a VO_2(M)–Ag–SiO_2 shell/core structured composite.

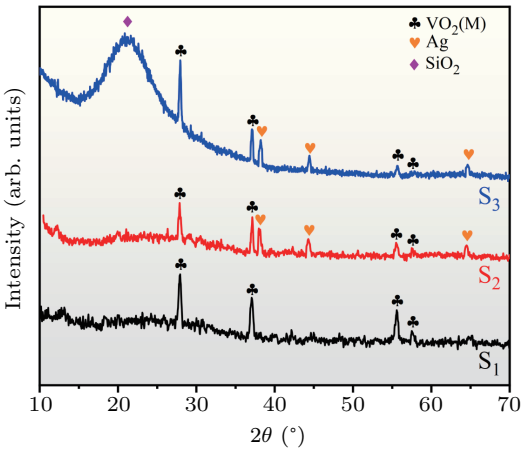


Fig. 2. GIXRD patterns of the samples. S_1, S_2, and S_3 correspond to the pure VO_2(M) film, the VO_2(M)–Ag composite film, and the VO_2(M)–Ag–SiO_2 composite film, respectively.

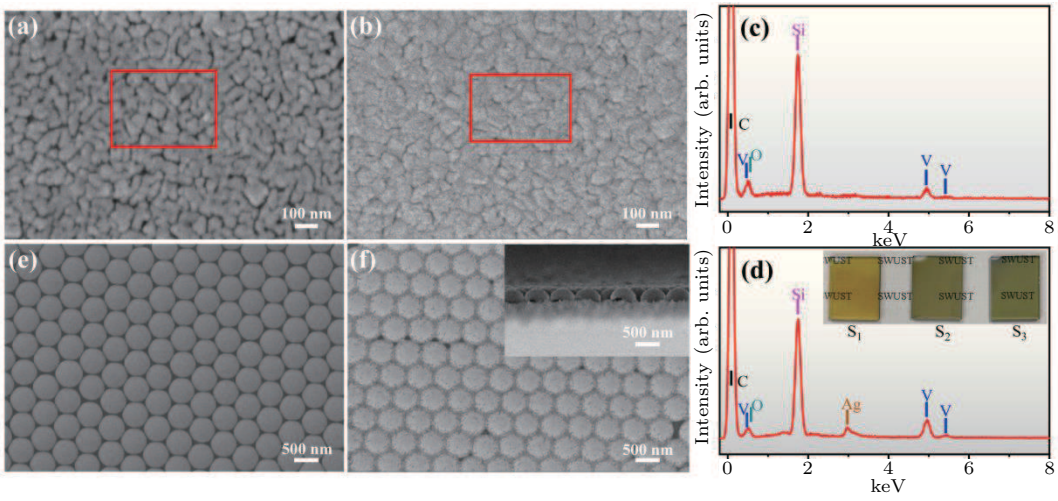


Fig. 3. FESEM images of all samples. (a) Pure VO_2(M) film, (b) VO_2(M)–Ag composite film, (c) and (d) EDS spectra corresponding to regions in (a) and (b), respectively. The inset in panel (d) shows a photograph of the samples. (e) Monolayer array of SiO_2 nanospheres, (f) VO_2(M)–Ag–SiO_2 composite film with inset showing a cross-sectional view.

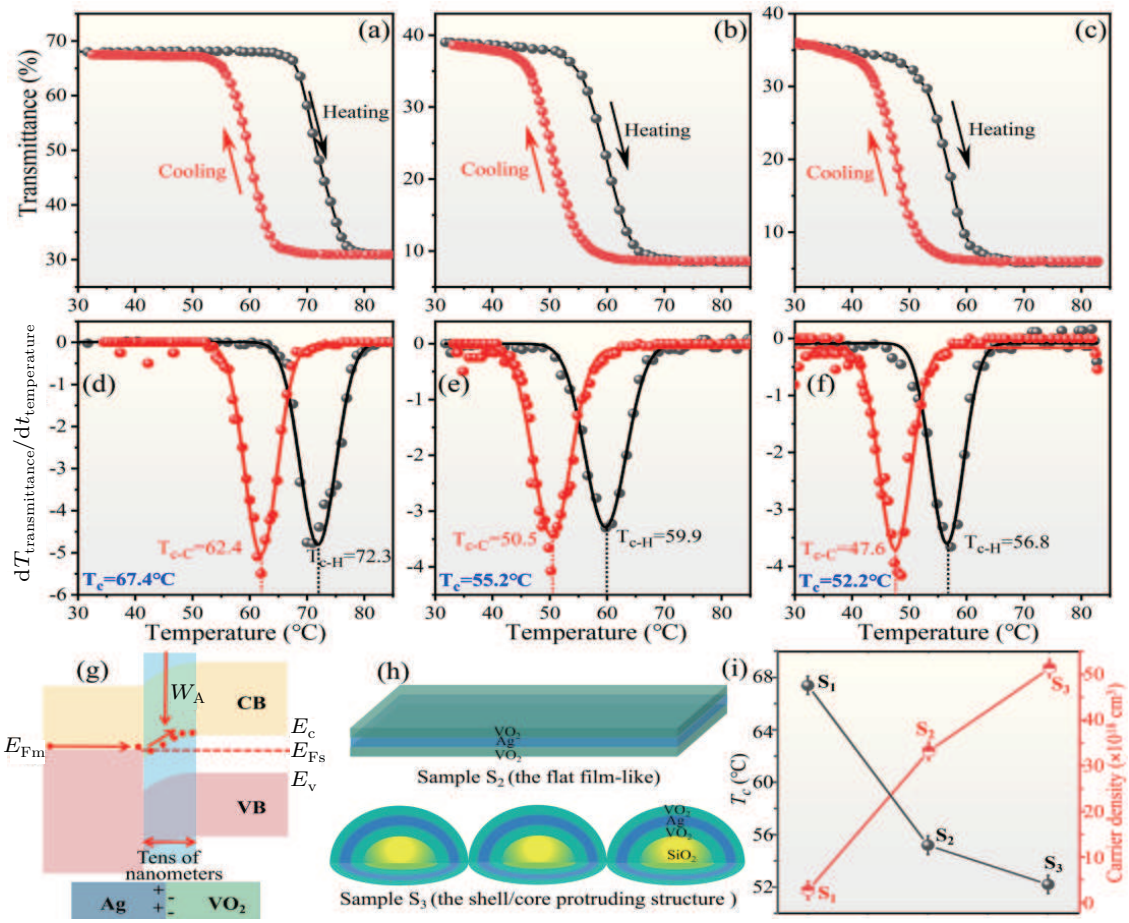


Fig. 4. (a)–(c) Temperature–transmittance hysteresis loops of samples S_1–S_3 measured at a wavelength of 2000 nm. (d)–(f) Corresponding first-order derivatives of the temperature–transmittance curves in panels (a)–(c). (g) Energy band diagram of Ag/VO_2. Red solid spheres indicate excited electrons. W_A denotes the energy absorbed in the Ohmic contact region during electron injection from Ag to VO_2. E_{Fm} and E_{Fs} represent the Fermi levels of Ag and VO_2, respectively, while E_c and E_v correspond to the conduction band and valence band of VO_2, respectively. (h) Schematic illustrations of the flat film-like structure (sample S_2) and the core-shell protruding structure (sample S_3). (i) Plots showing variations in phase transition temperature and carrier concentration for the samples.

To investigate the effect of Ag and SiO_2 arrays on the phase transition temperature (T_c) of VO_2(M), temperature-transmittance reversible hysteresis loops were measured at a fixed wavelength of 2000 nm, as shown in Figs. 4(a)–4(c). The heating and cooling paths are labeled as Heating and Cooling, respectively. Figures 4(d)–4(f) display the first derivatives of the thermal hysteresis loops for the S_1, S_2, and S_3 films. After incorporating Ag, the amplitude of the hysteresis loop is notably reduced, which is attributed to the strong absorption from surface plasmon resonance of the Ag particles in the visible to near-infrared region.[12,37,38] To accurately determine T_c, the Gaussian method was applied to obtain T_{c-H} and T_{c-C} during heating and cooling, respectively. Here, the critical temperature for the semiconductor-to-metal transition is defined as the midpoint of the thermal hysteresis loop

$$T_c = \frac{T_{c-H} + T_{c-C}}{2}. \tag{4}$$

According to Eq. (4), the T_c for S_1, S_2, and S_3 are calculated to be 67.4 °C, 55.2 °C, and 52.2 °C, respectively.

The significant reduction in T_c after introducing Ag can be explained by the theory proposed by Zylbersztejn and Mott.[12,34,39] Since the work functions of Ag and n-type VO_2(M) are 4.63 eV and 5.4 eV, respectively, the contact between Ag and the VO_2(M) film forms an Ohmic junction (Fig. 4(g)). In this case, free electrons flow from Ag to VO_2(M) until the Fermi levels (E_{Fm} and E_{Fs}) align. These injected electrons absorb additional energy (W_A) at the metal-semiconductor interface, thereby facilitating the phase transition at a lower temperature.[12,34,39] The T_c of S_3 is lower than that of S_2 because the shell/core protruding Ag structure in S_3 provides a much larger contact area with VO_2(M) than the flat film-like Ag in S_2 (Fig. 4(h)). Considering that the effective electron injection depth from Ag into the VO_2(M) film is only several tens of nanometers,[12] increasing the contact area effectively increases the number of injected electrons. Hall measurements at room temperature (Fig. 4(i), red dashed line) reveal carrier concentrations of 2.67×10^{18} cm^{-3}, 33.23×10^{18} cm^{-3}, and 51.38×10^{18} cm^{-3} for S_1, S_2, and S_3, respectively. This further confirms that, with the same Ag content, the VO_2(M)–Ag composite in S_3 embedded within the SiO_2 array substantially increases the Ag/VO_2(M) contact area, enabling more efficient electron injection from Ag

to VO_2(M) and consequently further reducing T_c.

Figure 5(a) shows the transmittance spectra of all samples within the 350–2500 nm range at 25 °C and 90 °C. Due to the strong inherent absorption of VO_2(M) in the short-wave region, the samples exhibit higher transmittance in the near-infrared range compared to the visible range.[13] All samples show high dynamic modulation capabilities in the near-infrared, with a marked transmittance contrast in this region between the two temperature states. At low temperatures, the films are relatively transparent to near-infrared light; while at high temperatures, they effectively block near-infrared transmission.[13] The behavior further confirms the presence of VO_2(M) within the films. Notably, at low temperatures, the transmittance of S_1 is significantly higher than that of the composite films, which can be attributed to the unique localized surface plasmon resonance properties of noble metal nanoparticles that strongly absorb light in the visible to near-infrared range.[12,37] As shown in Fig. 5(b), the absorption spectra of the composite materials S_2 and S_3 at room temperature and high temperature are significantly higher than that of S_1. Compared to composite film S_2, the room-temperature transmittance spectrum of S_3 exhibits a distinct dip around 600 nm. The effect is attributed to the two-dimensional diffraction grating properties of the VO_2(M)–Ag–SiO_2 shell/core monolayer structure, which strongly scatters light at specific wavelengths, thereby reducing transmittance.[24–27] Additionally, the structure exhibits unique structural coloration, allowing for color modulation.

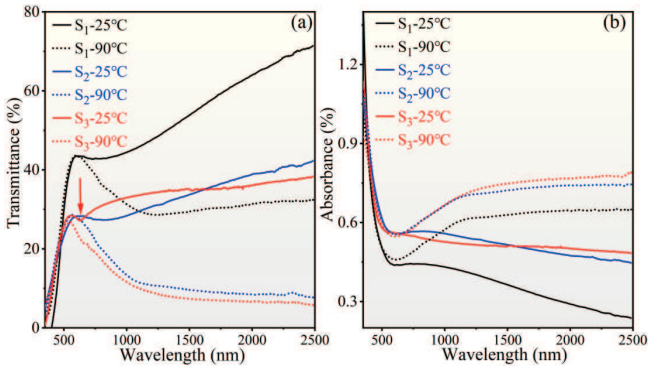


Fig. 5. Measured optical spectra of samples S_1–S_3 in the wavelength range of 350–2500 nm. (a) Transmittance spectra at 25 °C and 90°C. (b) Absorbance spectra at 25 °C and 90 °C.

The optical parameters of all samples were calculated based on Eqs. (1)–(3), and the results are summarized in Table 1. The T_{sol} of S_1 at 25 °C is 53.2%, and the ΔT_{sol} is 18.9%, which is consistent with the results reported by Hao *et al.*[39] For the composite materials, after embedding the SiO_2 nanosphere array, the ΔT_{sol} increases from 22.8% (S_2) to 25.4% (S_3), while the ΔT_{lum} increases by nearly 7 times (from 0.6% (S_2) to 4.3% (S_3)). By embedding SiO_2 arrays into VO_2(M)–Ag composite films to form a shell/core monolayer structure, the optical performance of the films in the visible light region is effectively tuned, achieving color modulation while significantly improving solar energy modulation efficiency.

Table 1. Optical properties of the produced films.

Sample	T_{lum} (%)		ΔT_{lum} (%)	T_{sol} (%)		ΔT_{sol} (%)
	25°	90°		25°	90°	
S_1	35.3	34.6	0.7	53.2	34.3	18.9
S_2	24.2	23.6	0.6	35.7	12.9	22.8
S_3	25.2	20.9	4.3	36.1	10.7	25.4

4. Conclusion

By the electron-beam evaporation method, a monolayer hexagonal close-packed SiO_2 array was successfully embedded into VO_2(M)–Ag composite film, forming a VO_2(M)–$AgSiO_2$ shell/core photonic crystal structure. Compared to the flat VO_2(M)–Ag composite film, the shell/core structure of the VO_2(M)–$AgSiO_2$ composite film increases the contact area between VO_2(M) and Ag, which facilitates the injection of more free electrons from Ag into VO_2(M), thereby further lowering the phase transition temperature to 52.2 °C. By embedding the SiO_2 array, the solar modulation efficiency of the film increases to 25.4%, and the visible light modulation efficiency rises by nearly an order of magnitude. Additionally, the film exhibits a grating effect, strongly diffracting light around 600 nm, which weakens the strong absorption of VO_2(M) in the short wavelength range due to electronic transitions, thus altering its inherent brownish-yellow color. These results provide valuable insights for the study of VO_2 films in smart windows, and further improvement of the film properties holds promise for commercial applications.

Acknowledgments

Project supported by the National Natural Science Foundation of China (Grant No. 12464004), Hubei Province Natural Science Foundation, China (Grant No. 2025AFB307), Hubei Province Natural Science Foundation Joint Fund Project (Grant No. 2024AFD069), Innovation Fund Project for College Students of Hubei Minzu University (Grant No. S202510517019), and Enshi Catching-up Science and Technology Project (Grants No. XYJ2023000170).

References

[1] Zhang Z, Zhang L, Zhou Y, Cui Y, Chen Z, Liu Y, Li J, Long Y and Gao Y 2023 *Chem. Rev.* **123** 7025
[2] Ma D, Yang T, Feng X, Wang P, Huang J, Wang J and Li H 2024 *Adv. Sci.* **11** 2307223
[3] Cui Y, Ke Y, Liu C, Chen Z, Wang N, Zhang L, Zhou Y, Wang S, Gao Y and Long Y 2018 *Joule* **2** 1707
[4] Chang T, Cao X, Long Y, Luo H and Jin P 2019 *J. Mater. Chem. A* **7** 24164

[5] Qin W, Yu T, Yang J, Li Z, Wu X, Fang Y and Song Y 2025 *Phys. Scr.* **100** 045546

[6] Vu T D, Chen Z, Zeng X, Jiang M, Liu S, Gao Y and Long Y 2019 *J. Mater. Chem. C* **7** 2121

[7] Li J H, Zhang Y T, Li J N, Li J, LI J T, Zheng C L, Yang Y, Huang J, Ma Z Z, Ma C Q, Hao X R and Yao J Q 2020 *Acta Phys. Sin.* **69** 22810 (in Chinese)

[8] Wang J L, Dong X C, Liang Y, Yang Z X, Wan H D, Chen H M and Zhou K 2023 *Acta Phys. Sin.* **72** 098101 (in Chinese)

[9] Fan L, Chen C, Zhu L and Zhang Q 2025 *Thin Solid Films* **815** 140639

[10] Matsuda Y H, Nakamura D, Ikeda A, Takeyama S, Suga Y, Nakara H and Muraoka Y 2020 *Nat. Commun.* **11** 1842

[11] Chen X, Wu M, Liu X, Wang D, Liu F, Chen Y, Yi F, Huang W and Wang S 2019 *Nanomaterials* **9** 834

[12] Zhou Z, Li J, Xiong Z, Cao L, Fu Y and Gao Z 2020 *Sol. Energy Mater. Sol. Cells* **206** 110303

[13] Hong K T, Moon C W, Suh J M, Lee T H, Kim S, Lee S and Jang H W 2019 *ACS Appl. Mater. Interfaces* **11** 11568

[14] Shen Y, Xu X, Sun M, Zhou W and Chang Y 2024 *Chin. Phys. B* **33** 044203

[15] Ke Y, Wen X, Zhao D, Che R, Xiong Q and Long Y 2017 *ACS Nano* **11** 7542

[16] Xu H, Guo X, Wang S, Liu T, Nie Y, Yang S and Jiang X 2023 *Appl. Surf. Sci.* **622** 156951

[17] Zhang L, Sun H, Liu H, Dong C, Li C, Mi W, Wang D, He L and Zhou L 2025 *Appl. Phys. A* **131** 222

[18] Li B, Liu J, Tian S, Liu B, Yang X, Yu Z and Zhao X 2020 *Ceram. Int.* **46** 2758

[19] Ke Y, Balin I, Wang N, Lu Q, Tok A, White T, Magdassi S, Abdulhalim I and Long Y 2016 *ACS Appl. Mater. Interfaces* **8** 33112

[20] Chen Y, Zeng X, Zhu J, Li R, Yao H, Cao X, Ji S and Jin P 2017 *ACS Appl. Mater. Interfaces* **9** 27784

[21] Xie Y, Zhao X, Mofid S, Tan J, Jelle B and Yang R 2021 *Mater. Today Nano* **13** 100102

[22] Liang J, Li P, Song X and Zhou L 2017 *Appl. Phys. A* **123** 794

[23] Men D, Liu D and Li Y 2016 *Sci. Bull.* **61** 1358

[24] Ye X and Qi L 2011 *Nano Today* **6** 608

[25] Aguirre C, Reguera E and Stein A 2010 *Adv. Funct. Mater.* **20** 2565

[26] Kang L, Gao Y, Chen Z and Du J 2010 *Sol. Energy Mater. Sol. Cells* **94** 2078

[27] Zhang X, Wang W, Zhao Y, Hu X, Reinhardt K, Knize R and Lu Y 2012 *Appl. Phys. A* **109** 845

[28] Li M, Ji S, Pen J, Wu H, Zhong L, Wang Q, Li F and Li G 2014 *J. Mater. Chem. A* **2** 48

[29] Kang L, Gao Y, Luo H, Wang J, Zhu B, Zhang Z, Du J, Kanehira M and Zhang Y 2011 *Sol. Energy Mater. Sol. Cells* **95** 3189

[30] Ye X, Huang J, Zeng Y, Sun L, Geng F, Liu H, Wang F, Jiang X, Wu W and Zheng W 2017 *Nanomaterials* **7** 291

[31] Josh C, Choudhuri M, Raya M, Chowdhury D, Chattopadhyay P and Datta A 2018 *Mater. Today Proc.* **5** 10143

[32] Zhou Z, Yang J, Liu Y, Gao Z, Cao L, Fang L, He H and Xiong Z 2021 *Chin. Phys. B* **30** 126803

[33] Vu T, Chen Z, Zeng X, Jiang M, Liu S, Gao Y and Long Y 2019 *J. Mater. Chem. C* **7** 2121

[34] Li M, Magdassi S, Gao Y and Long Y 2017 *Small* **13** 1701147

[35] Liang C, Zhang Y, Yi Z, Chen X, Zhou Z, Yang H, Yi Y, Tang Y, Yao W and Yi Y 2019 *Results Phys.* **15** 102635

[36] Du Z, Li M, Zou F, Song Y, Xu S, Wu L, Li L and Li G 2022 *ACS Appl. Nano Mater.* **5** 12972

[37] Zylbersztejn A and Mott N 1975 *Phys. Rev. B* **11** 4383

[38] Xu G, Huang C, Tazawa M, Jin P and Chen L 2009 *Opt. Commun.* **282** 896

[39] Hao Q, Li W, Xu H, Wang J, Yin Y, Wang H, Ma L, Ma F, Jiang X, Schmidt O and Chu P 2018 *Adv. Mater.* **30** 1705421